Aerodynamic-whistles-based ultrasonic tone generators for bat deterrence

Z. Zeng[1] and A. Sharma[1]

Department of Aerospace Engineering, Iowa State University,
537 Bissel Road, Ames, Iowa, USA 50011

(*Electronic mail: sharma@iastate.edu.)

(Dated: 14 August 2023)

Novel ultrasonic bat deterrents based on aerodynamic whistles are proposed and investigated experimentally and numerically for their ability to generate ultrasound. The baseline deterrent, a single-whistle design inspired by B. B. Beeken, "Fluid ultrasonic generator", 1969. US Patent 3,432,804[1], is examined first. It consists of two resonating cavities/chambers. The whistle is "powered" by a regulated high-pressure air supply and the performance of the whistle is examined for a range of supply pressures. Far-field acoustic measurements in the 20 Hz - 50 kHz frequency range are made in an anechoic chamber. The noise measurements are supplemented with two- and three-dimensional unsteady Reynolds-averaged Navier-Stokes (uRANS) simulations to investigate the mechanisms of ultrasound generation. The Ffowcs Williams-Hawkings acoustic analogy is used with the three-dimensional uRANS results to predict the far-field radiation. The far-field acoustic predictions are in good agreement with the measurements in the anechoic chamber. The peak frequency (fundamental) of the radiated ultrasound of the baseline deterrent is approximately 23 kHz. Harmonics and a sub-harmonic of the fundamental tone are also observed. The numerical simulations show that the two resonating chambers of the baseline deterrent operate out-of-phase and Helmholtz resonance determines the whistling frequency over the range of supply air pressure considered.

A six-whistle deterrent targeting a broad spectral coverage in the $20 - 50$ kHz frequency range is designed, fabricated and tested in the anechoic chamber. Each whistle in the deterrent is obtained by geometrically scaling the baseline whistle. Measurements show that the six-whistle ultrasound deterrent generates ultrasound with six dominant peaks in the designed frequency range when the supply air pressure exceeds 5 psig. The proposed ultrasound devices can be used for a variety of purposes including bat deterrence at wind turbines.

I. INTRODUCTION

Growth in wind energy has been driven in part by improvements in turbine design, e.g.,[2–4], and by numerical methods that enable such designs, e.g.,[5–8]. For wind energy to be a truly renewable energy resource however, this growth has to occur in an ecologically responsible manner. Bat mortality at wind farms is now recognized as a serious threat to the bat population and is a serious impediment to the future growth of wind energy in the world. Combined with the current environmental threats to bats (i.e., White-nose Syndrome), this added cause of mortality is pushing certain species of bats towards extinction[9–11]. Several strategies to mitigate bat mortality at wind farms are being pursued. These include (a) operational mitigation[12], which involves curtailing power generation, typically at low wind speeds, and (b) deterring bats away from wind farms using a variety of strategies, including ultrasonic deterrents[13–15], ultraviolet lights[16], and textured paints on turbine towers[17]. A serious drawback of curtailment is the associated loss of wind energy capture. Bat deterrents can significantly reduce (potentially eliminate) the need for curtailment and hence can serve as an alternate, more efficient approach. While results of initial testing with such deterrents look promising[13], the long-term effectiveness of these deterrents remains to be conclusively proven. Combinations of different

technologies, such as curtailment and ultrasonic deterrents, have also been explored[18].

Ultrasonic deterrence works by "jamming" the echolocation signals of bats, which is achieved by creating high-amplitude ultrasound. The ultrasound can be either broadband (white noise) or tonal. Schirmacher[19] verified that ultrasonic deterrents with a *tonal spectrum* (as opposed to broadband) are also effective at driving bats away. The intensity of the radiated ultrasonic tones can be increased by concentrating the acoustic power into a few frequencies (tones).

Current ultrasonic deterrents utilize electromechanical transducer-driven speakers[20] to generate ultrasound. These deterrents can be mounted on the turbine nacelle and tower. One example of such a deterrent is the Bat Deterrent System (BDS) developed by NRG Systems[19]. One unit of this system consists of six sub-arrays, each using multiple transducers to generate tonal ultrasound at a predetermined frequency. For example, a BDS could target 20, 26, 32, 38, 44 and 50 kHz frequencies. A six-tone BDS was found to be effective in mitigating bat fatality[19]. However, such electromechanical devices suffer from the following: (a) they require external power, which limits the possible mounting positions of the devices to the nacelle and the tower, and (b) maintenance issues due to rain/water and lightning damage. Aerodynamic ultrasound deterrents have also been pursued[14], where compressed air is accelerated in a nozzle and ejected as a supersonic jet. The noise such a jet produces is in the ultrasound range, and a broadband spectrum in the frequency range of $20 - 100$ kHz is generated. The compressed air supply source for such a system has to be housed in either the turbine tower or the nacelle.

Tonal ultrasound can be efficiently generated by using aerodynamic whistles. An aerodynamic whistle is a self-sustaining oscillator that can generate high-amplitude acoustic tones[21]. The dominant sound frequency of such a whistle is determined by its feedback mechanism. Based on the feedback mechanism, Chanaud[21] classified aerodynamic whistles into three classes. In Class-I whistles, the flow instability provides the feedback directly. The feedback is provided by the sound generator in Class-II whistles; in Class-III whistles, the feedback is provided by the resonator/sound reflector.

Flow-excited resonance, or whistling, has been studied extensively to understand sound generation mechanisms. A jet of fluid passing through a confined space is an aerodynamic whistle. It is observed in nature. For example, humans can whistle by blowing or sucking air through a small opening to the mouth with the lips, which produces *hole tones* with the mouth cavity acting as a Helmholtz resonator[22]. The whistle frequency can be adjusted by changing the tongue's position and shape and modifying the resonating mouth cavity. This phenomenon has been experimentally investigated by Wilson et al.[23].

Flow over a cavity also generates noise. Depending on the conditions, cavity noise can be a Class II or a Class III whistle. Gloerfelt[24] identified the possible mechanisms of cavity noise to be (i) Rossiter modes[25], which occur because of the acoustic feedback generated when the free shear layer over the cavity interacts with its downstream edge (ii) Helmholtz resonance, which is due to the compressibility of the fluid in the cavity, and (iii) standing-wave resonance in the cavity (depth, longitudinal and spanwise modes). Rossiter modes are associated with Class II whistles, while Helmholtz and standing-wave resonance are Class III. In some cases, Helmholtz resonance can exist simultaneously with standing wave resonance in a cavity[26].

Whistles are used in air-driven sound generation devices such as the steam/tea kettle. Through experiments, Henrywood and Agarwal[27] showed that the whistling mechanism in a tea kettle changes with the flow condition. At low Reynolds numbers (*Re*), the mechanism is Helmholtz resonance, which exhibits a near-constant frequency behavior. At high *Re*, the sound generation is due to vortex shedding (constant Strouhal number) at the orifice coupled with the upstream duct (spout) modes. In a classic Helmholtz resonator, the bottle "neck" is clearly defined; however, for cavities with thin walls (wall thickness $\ll$ cavity opening, such as the design considered in this work), the neck is not well defined, and an equivalent neck length should be used. Kinsler et al.[28] and Ruijgrok[29] present ways to estimate the Helmholtz resonance frequency of thin-wall cavities.

While aerodynamic whistles are typically used to generate sounds in the human-audible frequency range (20 Hz - 20 kHz), the whistle geometry can be modified to generate ultrasound. This paves the way for de-

veloping ultrasonic deterrents using aerodynamic whistles. The advantages of ultrasonic deterrents based on aerodynamic whistles include design simplicity (no moving parts), low cost, and the potential for generating high-amplitude ultrasound with minimal power (air supply) requirements.

In this work, we investigate novel ultrasonic deterrents that can generate tonal spectra in the $20 - 50$ kHz frequency range. The novelty is in using aerodynamic whistles and resonance to generate high-amplitude ultrasound. The geometries of the whistles are tailored to restrict the tone generation in the desired frequency range. We first examine the acoustic performance of a baseline ultrasonic whistle design inspired by Beeken [1]. A systematic study is conducted to unveil the ultrasound generation mechanisms and quantify the acoustic performance of the baseline whistle. The investigations include laboratory tests in the fully anechoic chamber at Iowa State University (ISU), supplemented with numerical results. Numerical predictions of the radiated sound are obtained by coupling the near-field flow solution with an acoustic analogy. Next, we present a six-whistle deterrent design targeting multiple tones in the $20 - 50$ kHz frequency range. The deterrent is fabricated and tested in the ISU anechoic chamber. The measurements show that the deterrent can readily generate the desired frequency spectra.

II. ULTRASOUND WHISTLE: BASELINE DESIGN

Figure 1a shows an exploded view of the baseline ultrasound whistle. The whistle consists of three parts: 1) a panel on which the flow channel is engraved, 2) a cover, and 3) a circular pipe to supply pressurized air. These parts are 3D printed using clear resin to fabricate the whistle models used in the experiments reported in this work. Pressurized air enters the whistle through the supply pipe, passes through the throat of the channel, over the orifices of the two resonating chambers, and leaves the whistle through the exit pipe. The fundamental frequency of the whistle is expected to stay constant over a wide range of supply air pressures[1]. By selecting proper physical dimensions, the whistle can generate tones in the ultrasonic frequency range (> 20 kHz). The working hypothesis is that this is a Class III whistle where the potential resonance mechanism is cavity noise (Helmholtz resonance, Rossiter modes, and standing waves) in the two resonating chambers.

The geometry of the flow channel determines the acoustic performance of the whistle. The key geometric parameters are identified in Fig. 2; Table I lists their dimensional values. The whistle is sized to have a fundamental frequency between $22 - 25$ kHz.

TABLE I: Key parameters of the whistle design (all lengths are in mm)

$L_{channel}$	L_{conv}	L_{res}	$L_{chamber}$	L_{pipe}	t	O	$R_{chamber}$	$D_{channel}$
65	25	11	6.4	6.4	1.6	2.4	2.4	2

III. METHODS

A. Experimental

The anechoic facility at ISU is a fully-anechoic chamber with a wire-mesh floor to support testing equipment. The test section dimensions are $15' \times 15' \times 12'$ (Fig. 3a). The noise floor in the chamber is 20 dBA, and the pressure transmission coefficient is 3×10^{-4}. The facility has been calibrated for free-field radiation in the chamber (see Fig. 3b).
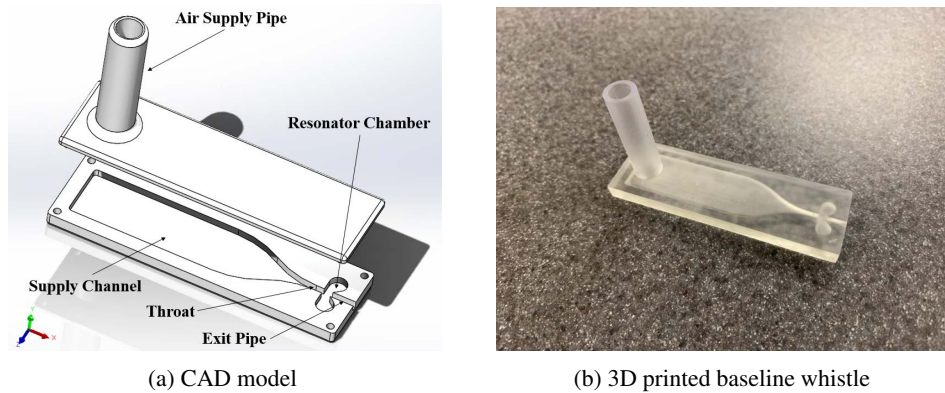
(a) CAD model

(b) 3D printed baseline whistle

FIG. 1: The ultrasound baseline whistle design following Beeken [1]. (a) CAD model, and (b) a 3D-printed model of the baseline whistle.
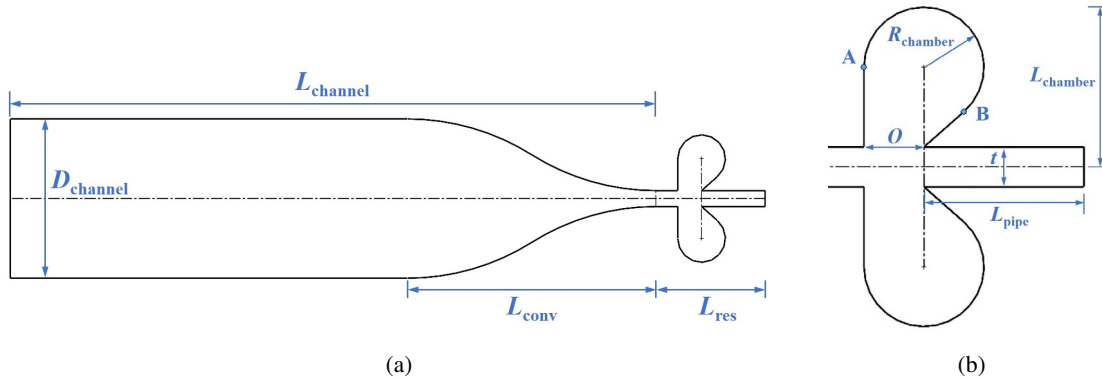

(a)

(b)

FIG. 2: Parameterization of the flow channel (in panel (a)) and resonating chambers (in panel (b)) of the baseline whistle. The dimensions are provided in Table I.

Acoustic measurements are made using quarter-inch, free-field, B&K 4939 microphones. The microphones are connected to a B&K 2690 conditioning amplifier, which supports simultaneous measurements over two channels. The B&K 2690 is connected to an NI PXIe 1073 data acquisition (DAQ) system. The B&K 4939 microphone has a dynamic range of up to 164 dB and a frequency range of 4 Hz to 100 kHz. The highest output frequency of the B&K 2690 amplifier is 100 kHz. Thus spectral measurements up to a frequency of 50 kHz are possible. The output sensitivity of the amplifier is preset as 100 mV/Pa.

The measured data are processed using MATLAB. Fourier analysis is performed on the time-domain pressure signal acquired by the DAQ system to obtain the power spectral density (PSD) of pressure in the frequency domain. Tonal frequencies are identified from the PSD spectra. We also report sound pressure levels (SPLs) for the tones, which are obtained by integrating the PSD spectra over frequency bands (bandwidth 2 kHz) centered at the peak frequency of the corresponding tone. The same approach is used to process the data from experiments and numerical simulations. Five independent readings are taken for each experiment in the anechoic chamber to reduce uncertainty, and the averaged spectra are reported.

(a) ISU anechoic chamber
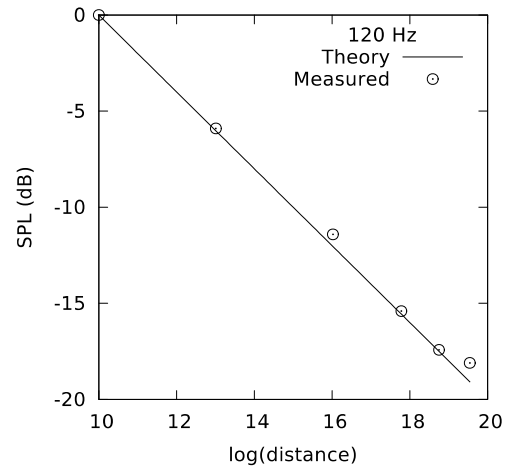
(b) characterization of the chamber

FIG. 3: The anechoic chamber facility at Iowa State University. (a) A deterrent model mounted in the anechoic chamber for acoustic testing, and (b) anechoic room soundproofing characterization, free-field radiation test result.

The deterrents are driven by compressed air. The laboratory air supply pressure is around 50 psig, which has to be reduced to lower pressures, between $0 - 10$ psig, for the deterrent devices tested. The supply air first passes through an oil/water filter for conditioning, followed by a flow control knob with a pressure gauge, and finally, through a high-precision volumetric flow-rate meter. The supply pressure and flow rate are recorded for each acoustic measurement. At the relatively low volumetric flow rates considered here (< 2 scfm), the flow speed in the air supply system is low enough that the measured supply pressure can be approximated as the stagnation pressure driving the whistle.

The deterrent is mounted in the center of the anechoic chamber. The microphones are positioned in a semi-circle of radius 1.651 m (see Fig. 3a) and are mounted every $15°$ along the arc to measure polar directivity (polar angle is measured from downstream of the whistle). The total radiated sound power level (PWL) is calculated by integrating the polar arc data over a sphere, assuming no azimuthal variation. The azimuthal variation in radiated ultrasound is much less pronounced than the polar variation (see Fig. 7).

B. Numerical

Aeroacoustic predictions are carried out using a two-step process wherein the acoustic sources are obtained in the first step via unsteady computational fluid dynamics (CFD) simulations. In step two, ultrasound radiation to the far field is obtained using the Ffowcs Williams-Hawkings (FW-H) acoustic analogy[30]. The STAR-CCM+ software is used for the CFD simulations. The numerical results supplement the radiating far-field acoustic measurements with near-field flow and acoustics information, which enables a comprehensive understanding of the flow and acoustic mechanisms involved. The simulations are performed in two and three spatial dimensions. Two-dimensional (2D) simulations are used for design studies, and three-dimensional simulations are used for verification against measurements. A mesh refinement study was performed to determine the appropriate mesh size for the simulations. The results are reported in Appendix

A.

Fluid flow is governed by equations that express the conservation of mass, momentum, and energy. This system of equations with an equation of state is called the Navier-Stokes (N-S) equations. We solve the unsteady Reynolds-averaged Navier-Stokes (uRANS) equations, obtained by density-weighted (Favre) short-time averaging the Navier-Stokes equations. Time averaging results in unresolved turbulent stress terms, which are modeled using a turbulence closure model. Transport equations for the turbulence kinetic energy (k) and specific dissipation rate (ω) are solved with appropriately-tuned production and dissipation terms via a $k - \omega$ turbulence model.

The density-weighted, short-time averaged N-S equations are

$$\frac{\partial \bar{\rho}}{\partial t} + \frac{\partial}{\partial x_j}(\bar{\rho} \tilde{u}_j) = 0, \tag{1}$$

$$\frac{\partial}{\partial t}(\bar{\rho} \tilde{u}_i) + \frac{\partial}{\partial x_j}(\bar{\rho} \tilde{u}_i \tilde{u}_j) = -\frac{\partial \bar{p}}{\partial x_i} + \frac{\partial}{\partial x_j}(\bar{\tau}_{ij} - \overline{\rho u_i'' u_j''}), \tag{2}$$

$$\frac{\partial}{\partial t}(\bar{\rho} c_p \tilde{T}) + \frac{\partial}{\partial x_j}(\bar{\rho} c_p \tilde{T} \tilde{u}_j) = \frac{\partial \bar{p}}{\partial t} + \tilde{u}_j \frac{\partial \bar{p}}{\partial x_j} + \overline{u_j'' \frac{\partial p}{\partial x_j}} + \frac{\partial}{\partial x_j}\left(\kappa \frac{\partial \tilde{T}}{\partial x_j} + \kappa \frac{\partial \overline{T''}}{\partial x_j} - c_p \overline{\rho T'' u_j''}\right) + \bar{\Phi}, \tag{3}$$

where the shear stress term $\overline{\tau_{ij}}$ can be written as

$$\overline{\tau_{ij}} = \mu\left[\left(\frac{\partial \tilde{u}_i}{\partial x_j} + \frac{\partial \tilde{u}_j}{\partial x_i}\right) - \frac{2}{3}\delta_{ij}\frac{\partial \tilde{u}_k}{\partial u_k}\right] + \mu\left[\left(\frac{\partial \overline{u_i''}}{\partial x_j} + \frac{\partial \overline{u_j''}}{\partial x_i}\right) - \frac{2}{3}\delta_{ij}\frac{\partial \overline{u_k''}}{\partial u_k}\right], \tag{4}$$

and the dissipation function $\bar{\Phi}$ can be written as

$$\bar{\Phi} = \overline{\tau_{ij}\frac{\partial u_i}{\partial x_j}} = \bar{\tau}_{ij}\frac{\partial \tilde{u}_i}{\partial x_j} + \overline{\tau_{ij}\frac{\partial u_i''}{\partial x_j}}. \tag{5}$$

In the above, the overline $(\bar{\ })$ denotes short-time averaging and the tilde $(\tilde{\ })$ represents density-weighted time-averaging. The superscript $''$ refers to the fluctuation of the mass-averaged variables. To close the system of equations, the Reynolds stress tensor $-\overline{\rho u_i'' u_j''}$ has to be modeled. This research uses the shear stress transport (SST) $k - \omega$ model[31].

1. Acoustic prediction

The Ffowcs Williams-Hawkings (FW-H) acoustic analogy is used to predict acoustic propagation to the far field from the near-field sources obtained from CFD. The FW-H formulation can be expressed in the following differential form.

$$\left(\frac{\partial^2}{\partial t^2} - c_o^2 \frac{\partial^2}{\partial x_i \partial x_i}\right)(H(f)\rho') = \frac{\partial^2}{\partial x_i \partial x_j}(T_{ij}H(f)) - \frac{\partial}{\partial x_i}(F_i \delta(f)) + \frac{\partial}{\partial t}(Q\delta(f)) \tag{6}$$

where,

$$\begin{aligned}
T_{ij} &= \rho u_i u_j + P_{ij} - c_o^2 \rho' \delta_{ij}, \\
F_i &= (P_{ij} + \rho u_i(u_j - v_j))\partial f/\partial x_j, \text{ and} \\
Q &= (\rho_o v_i + \rho(u_i - v_i))\partial f/\partial x_j.
\end{aligned} \tag{7}$$

Integration of Eq. 6 results in an unsteady mass addition (monopole) term corresponding to Q, an unsteady force (dipole) term corresponding to F_i, and an unsteady stress (quadrupole) term corresponding to T_{ij}. Since the flow speed is small, the volume-integral term corresponding to T_{ij} can be ignored. Therefore, only surface integrals must be computed on a surface that encloses all acoustic sources in the problem. Such a surface is often called a Kirchoff surface. Figure 4 shows the integration surface used in the current predictions. It consists of a "porous" surface, labeled 'Kirchoff surface 1' in the figure, which allows the flow to pass through it, and an impermeable surface, labeled 'Kirchoff surface 2'.
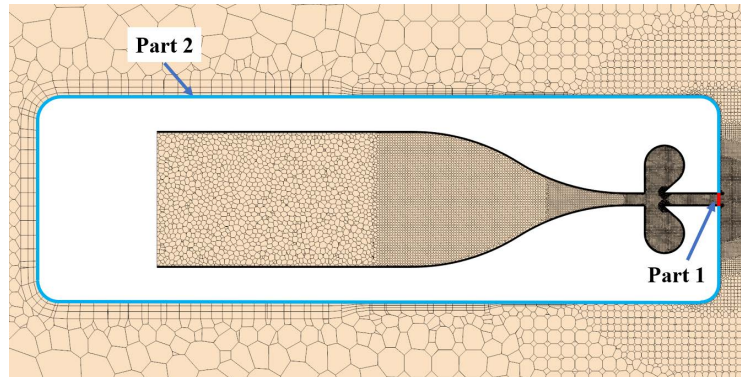

FIG. 4: The integration surface used to predict far-field ultrasound. The surface consists of a porous part (Kirchoff surface 1, shown in red) through which air can flow and an impermeable part (surface 2).

The numerical predictions must consider atmospheric absorption effects on sound propagation to compare with experimental measurements. The atmospheric absorption coefficients are calculated using the ANSI standard[32,33] for peak frequencies in the predicted spectrum with the temperature, relative humidity, and pressure set as 293 K, 50% and 1 atm, respectively.

IV. RESULTS AND ANALYSIS OF THE BASELINE WHISTLE

The baseline whistle is a Class-III whistle with resonating chambers acting as amplifiers. We aim to answer the following questions about this design: 1) what is the resonance mechanism at play (Helmholtz, Rossiter modes, pipe resonance, etc.)? 2) how does the fundamental frequency vary with supply air pressure/flow speed and resonator geometry? 3) how does the sound intensity vary with these variables? A combined experimental-numerical approach is taken to comprehensively analyze the whistle. The experiments are conducted in the anechoic chamber at ISU, and the numerical simulations are performed using the uRANS model described in section III B.

A. Experimental results

Figure 5 shows the far-field ultrasound radiation frequency spectrum from the baseline whistle for a supply air pressure, $p_t = 2.0$ psig. Figure 5a plots the power spectral density (PSD) of the pressure signal measured in the acoustic far field of the whistle. The baseline whistle has a fundamental frequency of around 23 kHz; harmonics of the fundamental frequency are also observed in the spectrum. A sub-harmonic at around ~ 11.5 kHz is also measured. The PSD spectrum can be integrated over a finite frequency bandwidth ($= 2$

kHz here) to obtain the tone sound pressure level (SPL). Figure 5b plots the SPL of the four tones measured in the frequency range $0-50$ kHz. The dominant peak at around 23 kHz has an SPL of over 90 dB (reference pressure is 20μ pa).

(a) PSD spectrum
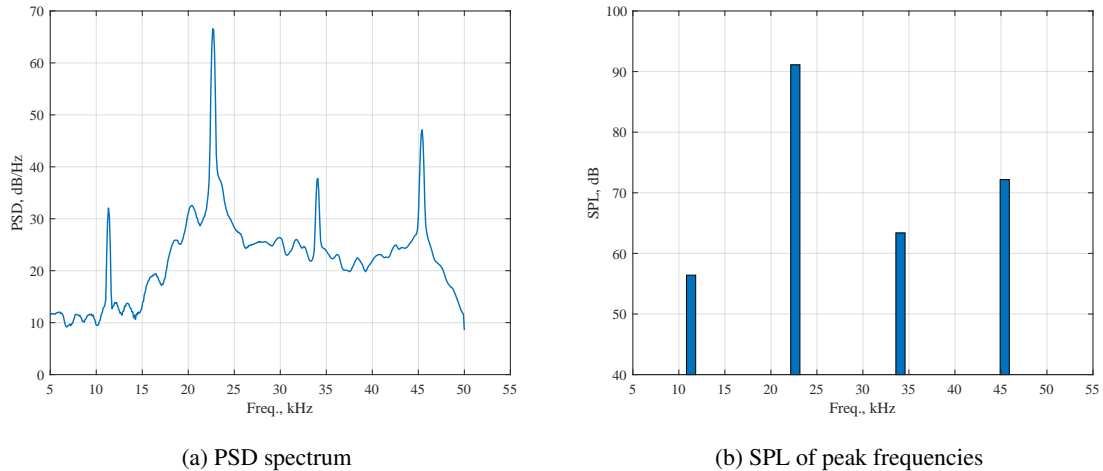

(b) SPL of peak frequencies

FIG. 5: Typical far-field sound spectrum of the baseline whistle, measured at supply pressure, $p_t = 2.0$ psig. (a) power spectral density (PSD) of pressure, and (b) sound pressure level (SPL) with reference to 20 μPa. The SPL computation requires integrating over a frequency band; the bandwidth used for integration is 2 kHz.

The measured far-field sound spectra for $0.3 < p_t < 2.5$ psig are plotted in Fig. 6. Such plots are called spectrograms wherein the variation of the frequency spectrum with time is considered; here, the variation is with p_t. In the pressure range considered here, the spectra show a fundamental (also peak) frequency between $20-24$ kHz. The peak frequency increases slightly with p_t. The first harmonic (between $40-48$ kHz) and a sub-harmonic ($10-12$ kHz) are also observed.

High-frequency sound can be highly directional. The directionality of sound radiation from the baseline whistle is investigated for one supply pressure value, $p_t = 2.0$ psig. Polar directivity is examined by mea-suring the sound signal along a 1.651 m arc, and azimuthal directivity is assessed by measuring at $0°$, $45°$ and $90°$ azimuthal angles. Figure 7 plots the directivity of the SPL of the peak frequency. As expected, the radiated sound is highly directional with maximum radiation occurring between polar angles $15°-45°$; note that the polar angle is measured from downstream of the whistle with the whistle-exhaust pointing at $0°$. The azimuthal variation (compare the three dashed lines with symbols in the figure) is much smaller, although not negligible. Five readings were taken to quantify the measurement uncertainty. The upper and lower bounds of the five readings are also plotted in Fig. 7 with thin lines of the same color. The measurement uncertainty ($\pm0.5 \times$ standard deviation) computed using five separate readings is shown with the shaded region bounded by thin solid lines.

B. Two-dimensional CFD analysis

To supplement the far-field acoustic measurements with flow field information, two-dimensional, unsteady fluid flow simulations are performed. The uRANS equations are solved with the $k - \omega$ SST turbulence
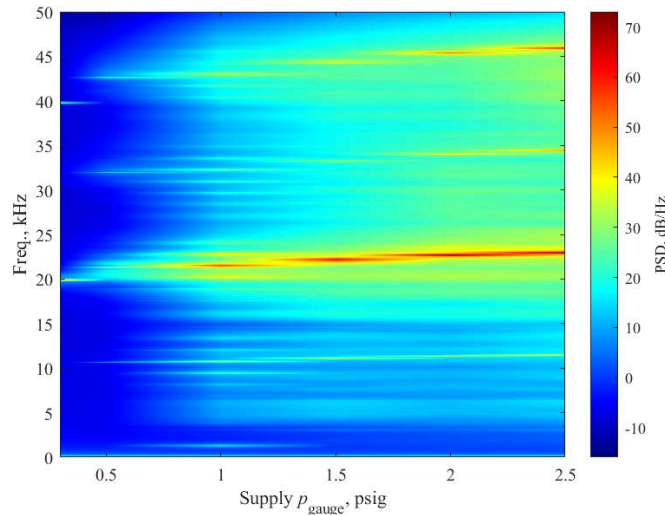
FIG. 6: PSD spectra variation with supply air pressure (p_t); this can be viewed as a spectrogram showing variation with p_t instead of time.

model in STAR-CCM+. Figure 8 shows the CFD domain, the mesh, and the boundary conditions used in the simulations. Adiabatic and no-slip wall conditions are applied on the side boundaries. Stagnation pressure is prescribed at the inlet boundary, and the outlet boundary is handled as follows. A large region (absorbing chamber) at the nozzle exit is included in the computational domain to allow for acoustic wave radiation out of the whistle (see Fig. 8a); the boundaries of the large region are prescribed to be at ambient pressure. Figure 8c provides a detailed view of the resonator and the whistle interface with the absorbing chamber.

Time-accurate data is collected at several (probe) locations inside the whistle and in the absorbing chamber. This data is processed to obtain the ultrasound spectra and directivity. Inside the whistle, a probe is placed along the centerline of the flow channel at the throat, and two probes are placed at the center of each resonating chamber. Outside the whistle, seven probes are placed in a circular arc of radius 30 mm centered at the whistle exit. The probe locations are illustrated in Fig. 9a.

Simulations are conducted over a range of inlet stagnation pressures ($0.1 \leq p_t \leq 2.5$ psig). The simulation result for $p_t = 2.0$ psig is discussed in detail here. Figure 9b shows the radiating sound field. Figure 10a plots the power spectral density of the acoustic pressure in the far field. The peak frequency of the radiating sound field is ~ 24 kHz. Harmonics and sub-harmonics of the peak frequency are also observed. The harmonics are beneficial for bat deterrence because they cover a wider ultrasonic frequency range. Since different bat species echolocate at different frequencies, multiple bat species can be targeted with a wider frequency coverage. The sub-harmonic tone is undesirable as it can fall in the human-audible range, as it does for the baseline deterrent. However, the magnitude of the sub-harmonic tone is small. The predicted spectrum qualitatively agrees with the experimental result in Fig. 5a.

The directionality of the radiated sound field can be inferred from Fig. 9b. Figure 10b is a polar plot of the pressure PSD of the peak frequency, which shows the peak radiation occurring at around $45°$ polar angle. This qualitatively agrees with the measurements (compare with Fig. 7, which show peak radiation off-axis, between $15° - 45°$ polar angle).

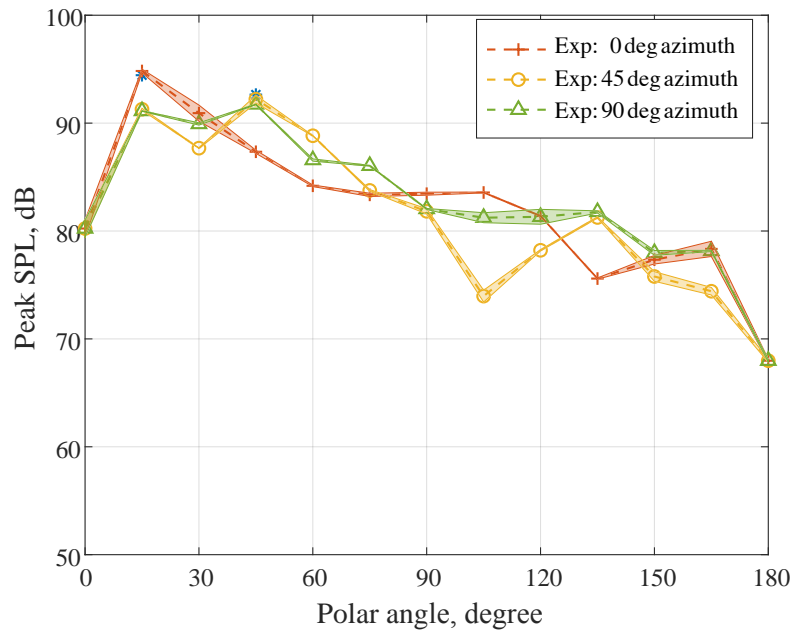Figure 11 contrasts the pressure PSD spectra at the center of Chamber A with that in the far field. The

FIG. 7: Directivity of sound radiation from the baseline whistle for three azimuthal angles - 0°, 45°, & 90°. Also shown with thin lines around each reading are the error bounds (one standard deviation) computed from five separate measurements.
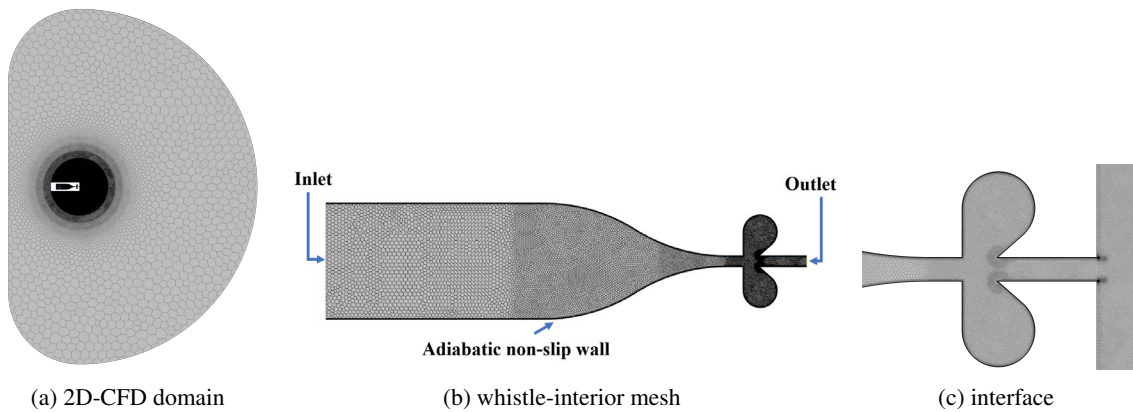

(a) 2D-CFD domain   (b) whistle-interior mesh   (c) interface

FIG. 8: The computational mesh used for 2D simulations. (a) overall domain showing the large absorbing chamber, (b) mesh inside the whistle, and (c) zoom view of the mesh in the resonators and near the whistle exit.

acoustic signal at the chamber center has a peak frequency of 12 kHz, which is half of the peak frequency of the radiating sound. Figure 12a provides a snapshot of the pressure field inside the two resonators, and Fig.

(a) probe locations
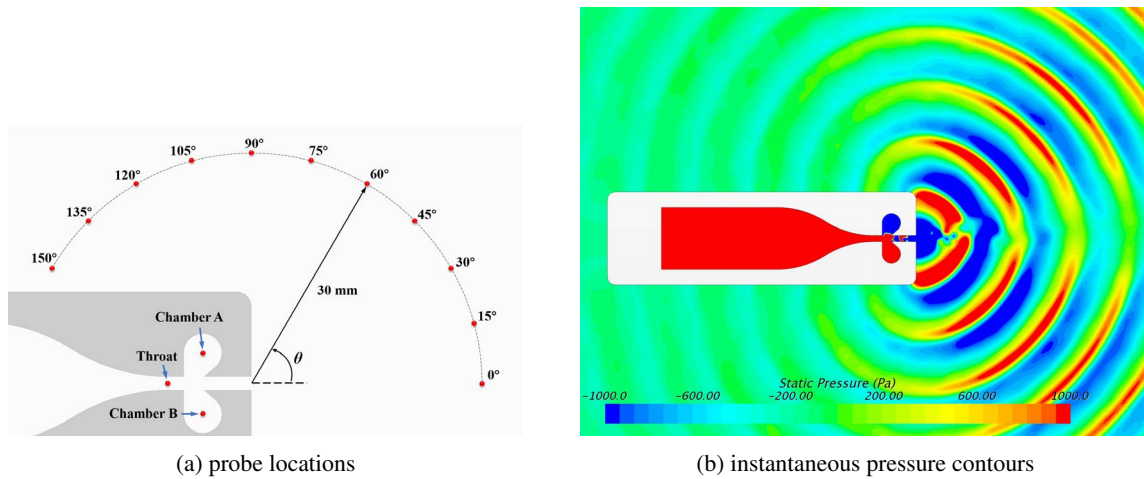

(b) instantaneous pressure contours

FIG. 9: Two-dimensional CFD analysis. (a) Probe locations where time-accurate data is collected for spectral analysis, and (b) visualization of the acoustic waves via pressure contours.

(a) PSD of radiated sound at $30°$ polar angle
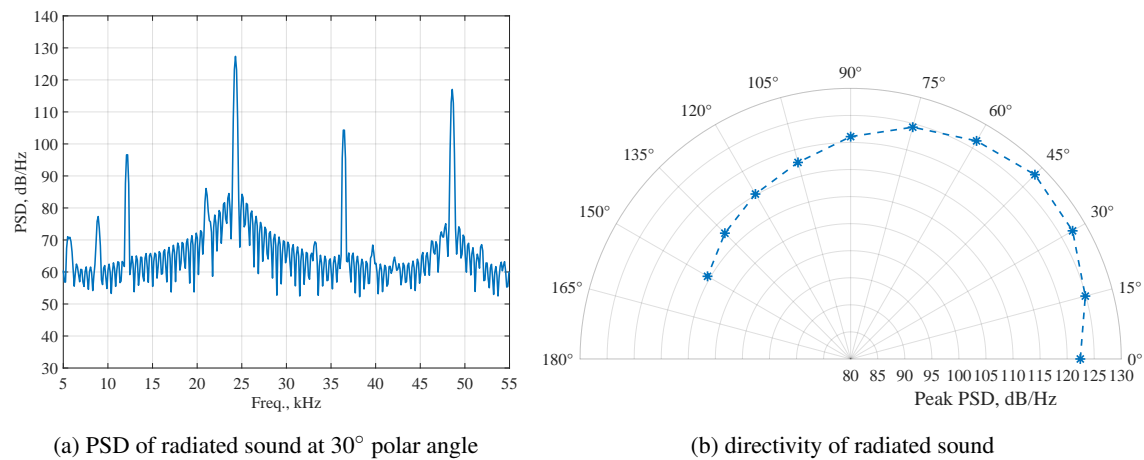

(b) directivity of radiated sound

FIG. 10: 2D CFD results of the baseline whistle for $p_t = 2.0$ psig. (a) PSD of the radiated pressure field, and (b) the far-field sound directivity

12b compares the time histories of the pressure at the center of the two chambers, which conclusively shows that the two chambers are operating out-of-phase. These results indicate that the basic mechanism of the baseline whistle is as follows. The chambers/resonators have a fundamental frequency of around 12 kHz. Since the chambers operate out-of-phase, the fundamental (and the odd harmonics) of the two chambers cancel each other, and the even harmonics radiate to the far field. Therefore, the second harmonic (~ 24 kHz) appears in the far field as the peak frequency. Since the phase cancellation is imperfect, some energy radiates in the fundamental and the odd harmonics.

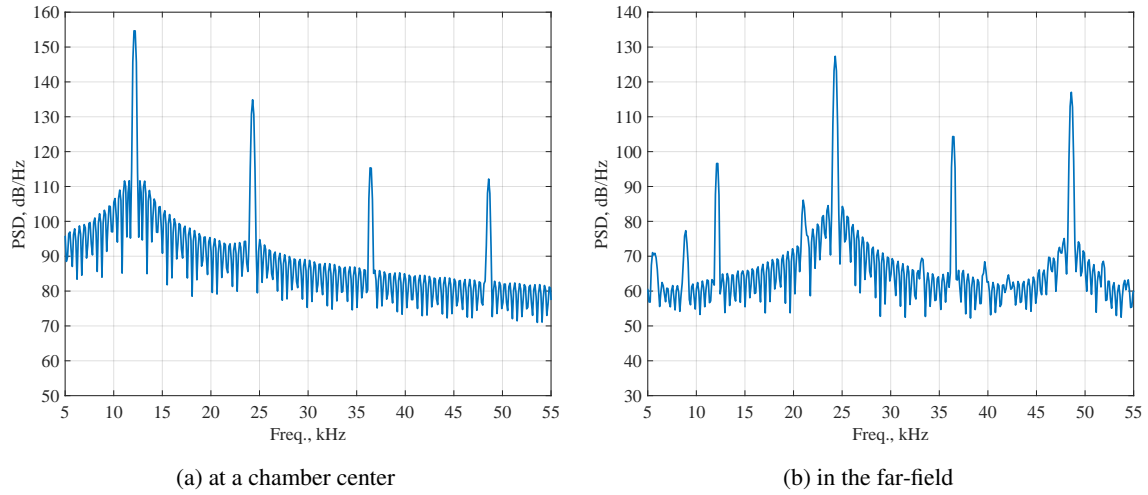We next investigate the performance of the baseline whistle with varying inlet (supply) pressure and

(a) at a chamber center

(b) in the far-field

FIG. 11: Comparison of pressure PSDs measured (a) at the center of one of the resonating chambers and (b) in the far-field

(a) Pressure field in the resonators

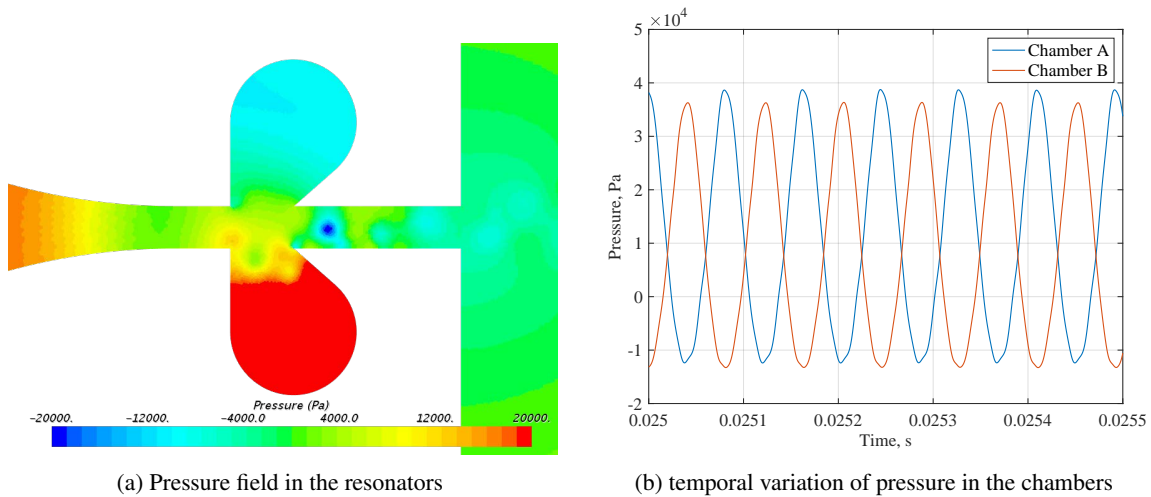(b) temporal variation of pressure in the chambers

FIG. 12: Out-of-phase pressure oscillation in the two chambers/resonators of the whistle: (a) pressure contours in the chambers, and (b) pressure signals at the centers of the two chambers.

geometry.

   a.   Variation with supply pressure   Two-dimensional CFD simulations of the baseline whistle are performed for several p_t values in the range $0.1 \leq p_t \leq 2.5$ psig. The results are summarized in Table II.

Variations with p_t of pressure PSD spectra in the far-field and at the center of one of the resonating chambers are plotted as "spectrograms" in Fig. 13. The numerical results in Fig. 13b are qualitatively

TABLE II: Summary of 2D CFD simulation results for varying p_t

p_t (psig)	avg. M at throat	peak chamber freq. (kHz)	peak far-field freq. (kHz)	phase relation between chambers
0.1	0.085	6.10	12.21	in-phase
0.3	0.142	9.77	19.65	out-of-phase
0.5	0.172	11.11	22.09	out-of-phase
0.8	0.165	11.11	21.36	out-of-phase
1.0	0.178	10.99	21.85	out-of-phase
1.2	0.162	11.11	22.09	out-of-phase
1.4	0.167	11.23	22.58	out-of-phase
1.6	0.169	11.47	22.83	out-of-phase
1.8	0.175	11.60	23.32	out-of-phase
2.0	0.163	12.08	24.29	out-of-phase
2.1	0.164	12.21	24.29	out-of-phase
2.3	0.163	12.21	24.41	out-of-phase
2.5	0.163	12.21	24.54	out-of-phase

similar to the corresponding experimental measurements in Fig. 6. Both show the peak frequency around 23 kHz, which increases slightly with p_t. In the results from both methods, there appears to be a threshold p_t value below which the whistle does not produce any tones or is "cut-off".

(a) chamber center
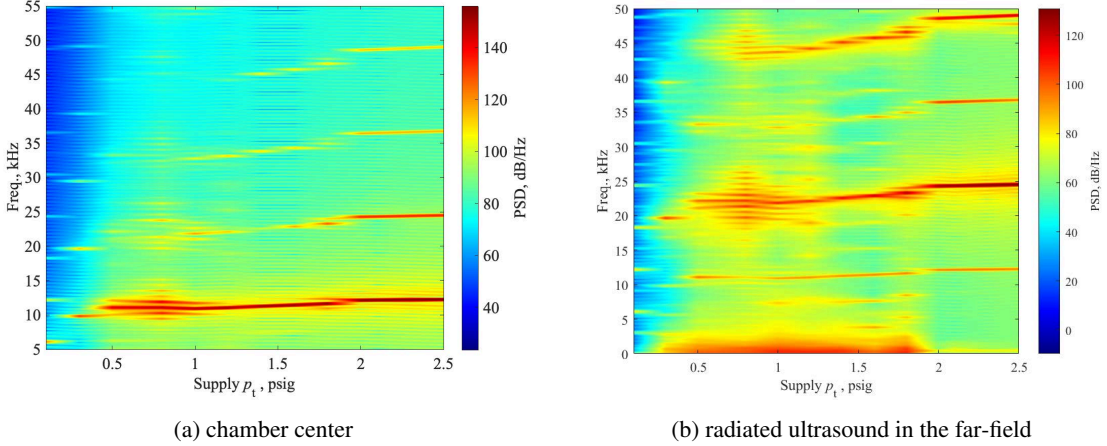
(b) radiated ultrasound in the far-field

FIG. 13: 2D CFD results of the baseline whistle. Variation of PSD spectra with p_t: (a) at the center of one of the chambers, and (b) 30 mm away from the whistle (in the far-field) at $30°$ polar angle.

Figure 14 compares the variations with p_t of peak frequencies at the center of one of the resonating chambers with that of the radiating far-field sound. Also plotted in the figure are curves corresponding to the frequencies associated with different sound generation mechanisms theoretically possible in the baseline whistle. These include Helmholtz resonance (H.R.), standing wave (S.W.) resonance, and Rossiter modes in the chamber. The closed-form expressions relating these frequencies to geometric and flow parameters are provided in Appendix B.

Figure 14 shows that the peak frequency in the resonating chambers closely follows the theoretical es-
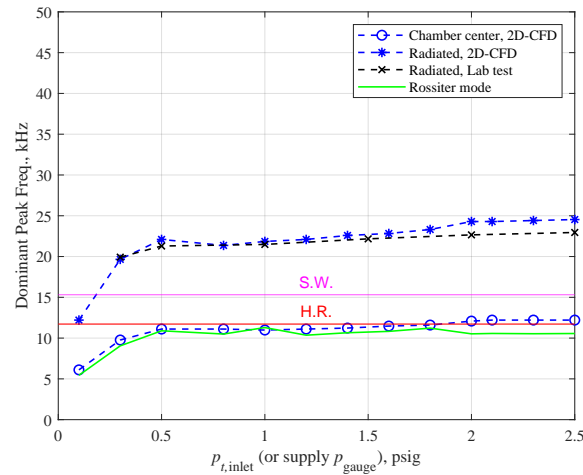
FIG. 14: Variations with p_t of peak frequencies in the far-field obtained from 2D CFD and measurements and in one of the chambers (from CFD). Also plotted are theoretical estimates of frequencies corresponding to Helmholtz resonance (H.R.), standing-wave (S.W.) resonance, and the first Rossiter mode.

timate of the first Rossiter mode. However, the frequency of the first Rossiter mode is very close to the Helmholtz resonance frequency for this design over the p_t range considered here (see Appendix B). Once resonance is established, the resonance-amplified signal (feedback) controls the flow instability and dictates the shear layer flapping frequency[24]. The observations, therefore, suggest that in the range of p_t evaluated here, the device operates as a Class III whistle with the first Rossiter mode and/or Helmholtz resonance amplifying the acoustic signal. To differentiate between Helmholtz resonance and Rossiter modes, we investigate a different whistle design where these frequencies are distinct; Appendix C presents the results of this study. We found that the peak frequency in the chamber is closer to the theoretical estimate of Helmholtz resonance than the first Rossiter mode. Hence, we conclude that Helmholtz resonance is the dominant amplification mechanism, although both Helmholtz resonance and Rossiter modes are at play for the baseline design.

Since the two chambers (resonators) operate out of phase, the sound radiated by the whistle into the far field is at double the Helmholtz resonance frequency, as seen in Fig. 14. The peak frequency increases slightly with p_t, which can be caused by the change in the geometry (likely the "effective" neck) of the resonator due to the variation in boundary layer thickness with p_t. At small p_t ($0.1 \leq p_t \leq 0.5$ psig), the peak frequency and the throat Mach number (M) increase with p_t. However, once p_t exceeds 0.5 psig, these quantities become insensitive to p_t. Note that while the peak frequency and M do not vary with p_t in this range, the peak SPL increases with increasing p_t.

b. Variation with whistle size   The peak frequency of the whistle can be altered by geometrically scaling the resonators. To target multiple frequencies in the 20 kHz to 50 kHz range, we investigate multiple designs obtained by geometrically scaling down the baseline whistle. The percentage scaling (based on linear dimension) considered here and the corresponding peak frequencies and SPL (obtained using 2D CFD) are tabulated in Table III.

Figure 15 shows the far-field pressure PSD spectra of three whistles that are 100%, 70%, and 50% the size of the baseline whistle. The results show that this set of whistles covers the 20 kHz to 50 kHz fre-

TABLE III: Peak frequencies and SPLs of several whistles obtained by geometrically scaling down the baseline whistle. The peak frequency and SPL are obtained from the pressure signal captured at a 30° polar angle, 30 mm away from the whistle exit.

size (% of baseline)	peak freq. (kHz)	peak SPL (dB)
100	24.29	151.34
85	28.44	150.31
70	34.55	149.01
60	40.16	146.60
55	43.82	145.22
50	48.10	143.02

quency range, which covers a majority of the bat species in North America adversely impacted by bat-turbine interaction[34].
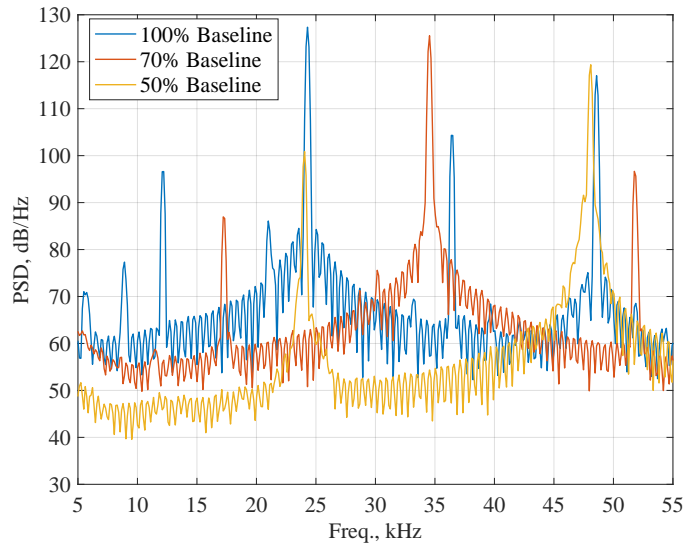

FIG. 15: 2D CFD predictions of far-field pressure PSD spectra of three whistles derived by scaling the baseline whistle

C. Three-dimensional aeroacoustic analysis and comparison with data

While the 2D simulations are helpful for qualitative understanding and design guidance, they cannot be quantitatively compared with experimental data. Three-dimensional (3D) simulations are therefore performed to validate the prediction approach. Figure 16 shows the mesh used for the 3D simulations of the baseline whistle. An absorbing chamber that surrounds the whistle is included in the domain to account for 3D acoustic radiation.

The boundary conditions for the 3D simulations follow the 2D simulations, with total pressure specified

(a) absorbing chamber   (b) mesh inside the whistle   (c) zoom view of the resonators
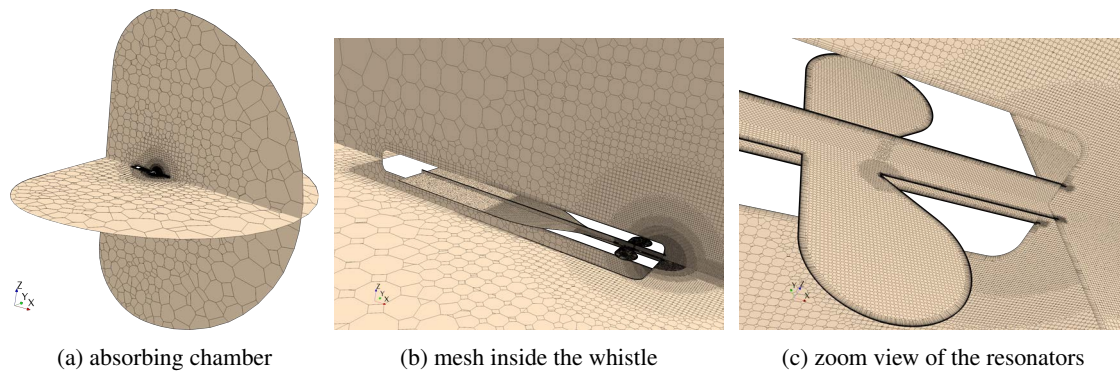
FIG. 16: Computational mesh for 3D CFD analysis of the baseline whistle: (a) overall mesh showing the acoustic/absorbing chamber, (b) mesh inside the whistle, and (c) zoom view of the mesh in the resonators.

at the whistle inlet, whistle surfaces treated as adiabatic, no-slip walls, and freestream conditions specified at the outer boundary. A nominal uniform flow speed of 1 m/s (along the whistle axis) is specified in the absorbing chamber to stabilize the simulation by ensuring that the boundary condition does not fluctuate between inflow and outflow due to small perturbations due to acoustics waves or numerical error. The freestream condition at the outer boundary of the absorbing chamber supports this uniform flow.

The numerical modeling approach is also the same as in the 2D simulations. The cell size increases rapidly in the absorbing chamber away from the whistle exit (see Fig. 16) to manage the total mesh size. Excessive numerical dissipation due to coarse grids does not permit accurate acoustic propagation to the far field in these numerical simulations. Therefore, the far-field acoustic radiation is obtained by solving the FW-H equation (Eq. 6). Figure 4 shows the FW-H integration surface. The observer locations at which the FW-H predicts the radiated sound are 1.651 m from the exit of the whistle, which is the same as the whistle-microphone distance in the measurements. The observers are distributed along a semi-circular array in 15° polar angle intervals.

Figure 17 compares the numerical acoustic predictions (using 3D CFD and FW-H) with the measured spectra at 30 deg polar angle and 1.651 m away from the whistle. Pressure PSD and tonal SPL spectra are compared in the figure. The predictions agree reasonably well with the measurements, particularly for the tonal SPL spectra. The simulations show a slightly higher peak frequency than the measurements, possibly due to differences in the whistles' modeled and fabricated geometries and supply pressure. Nevertheless, the peak amplitudes are quite close. The larger scatter in the simulations is because the averaging time for the simulated spectra is not as large as for the measured spectra.

Figure 18a compares the far-field polar directivity of peak SPL between simulations and experiments for a fixed azimuthal angle ($= 0°$). The predictions qualitatively capture the measured behavior – SPL decreases with increasing polar angle. However, the sharp reduction observed at 0° and 180° in the measurements is not seen in the predictions. This sharp reduction in radiated ultrasound along the axis in the experiments is a result of acoustic refraction due to whistle exhaust flow at 0°, and due to scattering/blockage by the whistle and the stand (to hold the whistle in place) at 180°. The FW-H acoustic radiation model does not include these refraction and scattering effects.

The power in the radiated ultrasound field is obtained by integrating the flux of acoustic power through a spherical surface surrounding the whistle. Figure 18b compares the radiated acoustic power PSD between the predictions and experiments. Atmospheric attenuation is accounted for in the simulations. The predicted radiated ultrasound power levels (SWL) are slightly higher than the measurements.

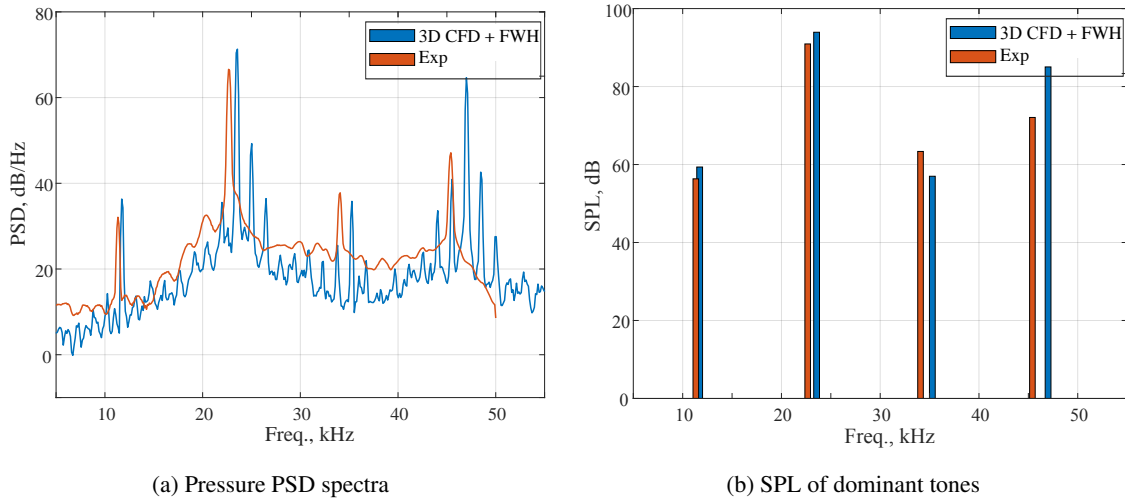(a) Pressure PSD spectra

(b) SPL of dominant tones

FIG. 17: Comparison of the radiating ultrasound between measurements in the anechoic chamber and numerical (3D CFD + FW-H) results: (a) pressure PSD spectra in the far-field at $30°$ polar angle, and (b) SPL of dominant tones

(a) directivity of the dominant peak

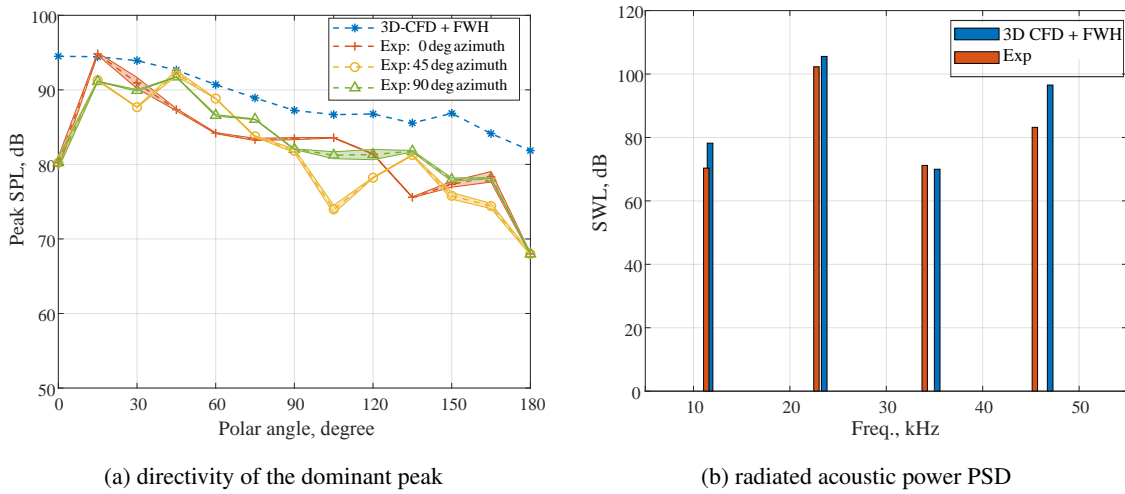(b) radiated acoustic power PSD

FIG. 18: Comparisons between 3D-CFD FWH and measurements (a) peak SPL polar directivity (at $0°$ azimuthal angle, 1.651 m from whistle exit), and (b) sound power level (SWL) spectra (wref E-12 W).

V. SIX-WHISTLE ULTRASOUND DETERRENT

An ultrasonic bat deterrent targeting multiple frequencies in the $20 - 50$ kHz range is developed based on the baseline whistle. It consists of six whistles obtained by geometrically scaling the baseline design. The whistles are scaled 100%, 85%, 70%, 60%, 55%, and 50% of the baseline along each dimension. All the

whistles are powered by one source of pressurized air. Since the throat area of the whistle determines the flow rate through it, the depth of the whistles are modified to ensure identical throat areas (3.2 mm^2) for the six whistles. For ease of fabrication, the six whistles are distributed into two sets, each containing three whistles (see Fig. 19). The two whistle sets are connected to a diffuser via a socket and pressurized air is supplied to the whistles through the diffuser. Each whistle set is 3D printed as one piece using clear resin. The diffuser and socket are 3D-printed using polylactic acid (PLA). Figure 19b is a picture of the fabricated deterrent. The different parts of the deterrent are assembled and held together using epoxy.

A significant advantage of this deterrent is its low cost. As we have done here, the deterrent can be fabricated with 3D printing using plastic (PLA) instead of machined metal and has a very simple design/structure. Therefore the production cost is much lower than that of transducer-based ultrasonic deterrents. Secondly, the proposed deterrent is readily driven by off-the-shelf air compressors; there is no need for delicate and fragile electronic transducers/controllers. The operational cost of this deterrent is therefore also expected to be lesser.

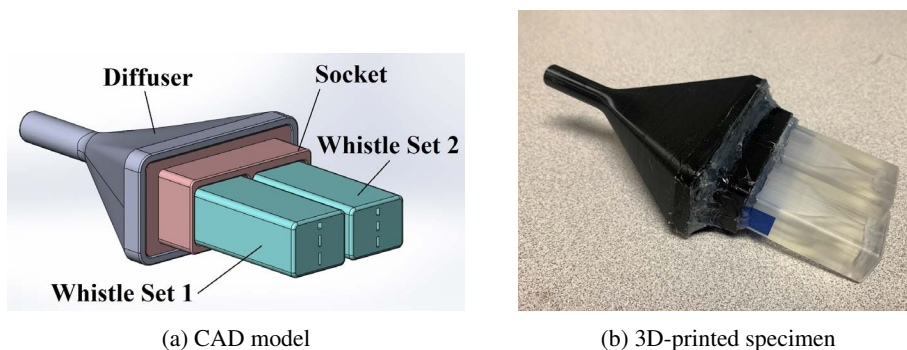(a) CAD model   (b) 3D-printed specimen

FIG. 19: A six-whistle active ultrasonic deterrent device. (a) a computer-aided design (CAD) model of the deterrent, and (b) the model fabricated using additive manufacturing (3D printing).

A. Experimental analysis of the six-whistle deterrent

The six-whistle deterrent is tested in the anechoic chamber using the same setup as the baseline whistle. The deterrent is expected to generate at least six major peak frequencies (see Table III). The acoustic performance of this deterrent is tested for supply pressure (p_t) of 2, 3, 4, 5, 7 and 10 psig. The microphone capturing the radiating sound is located at $30°$ polar angle. Figure 20a plots the far-field pressure PSD spectra for $p_t = 2$, 5, and 10 psig. It is seen that although a six-peak-pattern in the spectrum is established for $p_t \geq 5$ psig, the frequencies of the peaks (even at 10 psig), are slightly lower than the values expected from the isolated-whistle analysis.

Figure 20b shows the SPLs of the significant peaks for three values of p_t (=2, 5, 10 psig). At 10 psig, the six major peaks reach SPL values between $90 - 100$ dB, significantly higher than those at 5 psig. With higher supply pressure (50 psig possible with off-the-shelf air compressors), it is possible to match the ultrasound radiation levels (SPL $\sim$ 115 dB) of commercially available electromechanical transducer-based ultrasonic deterrents.

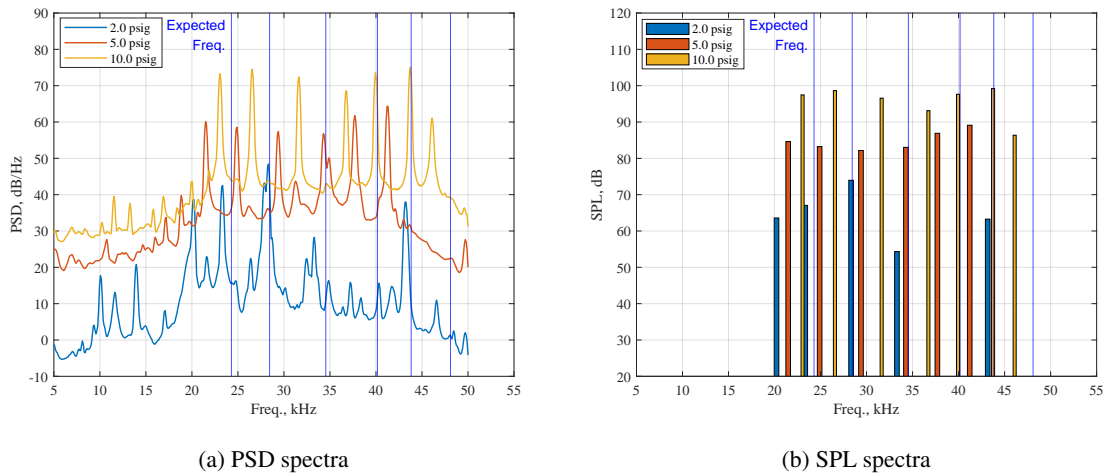(a) PSD spectra   (b) SPL spectra

FIG. 20: Experimental results of the six-whistle active ultrasonic deterrent for three supply air pressures.
(a) power spectral density (PSD) spectra, and (b) sound pressure level (SPL) spectra. Expected frequencies
from the isolated-whistle analysis are shown as vertical blue lines.

B.   Applications and implications of the proposed deterrent

Two prominent applications of the proposed deterrent are transportation and wind energy.

1. *Department of transportation (DOT)*. Continued destruction of bat habitats due to increasing human
   population is forcing the bats to seek alternative roosting options in roadway bridges and culverts.
   DOTs need a safe and effective way to exclude bats from these structures. Common methods for
   physically excluding bats on highway structures include installing escape tubes, netting or screens,
   expandable foam, and plywood. These methods are intrusive and can impact the structural integrity
   and appearance of the structures. Acoustic deterrents offer a non-intrusive way to achieve the same
   objective. Our proposed device is economical and is likely suitable for this purpose.

2. *Wind energy.* The proposed deterrent can be mounted on turbine tower and nacelle and powered
   by commercial off-the-shelf compressors that can be housed in the tower/nacelle. A passive, blade-
   mounted version of the deterrent can be used without the need for a compressor; however, such passive
   deterrents are beyond the scope of this paper.

The deterrent can also potentially be used in automobiles to ward off deer from their paths and avoid
collisions and consequent damage.

While the effectiveness *on bats* of the proposed deterrent remains to be tested, we believe that it should
elicit the same bat response as the NRG bat deterrent system (BDS) since both devices produce tonal ul-
trasound of similar intensity. Our deterrent can be tuned to produce any number of tones in the $20 - 50$
kHz range, similar to the NRG BDS. If the proposed device is effective at deterring bats, it has huge impli-
cations on the wind energy industry, civil infrastructure (bridges, etc.), and other public buildings (parking
lots) and private dwellings. While in the case of wind energy, these deterrents would serve to reduce bat
mortality, in other cases, it would be to avoid the nuisance (and potentially diseases) caused by bats roosting
in undesirable places.

VI. CONCLUSION

Numerical and experimental analyses of novel ultrasonic deterrents designed using aerodynamic whistles are presented. The baseline deterrent/whistle, which consists of two identical resonators, generates ultrasound with a peak frequency of around 24 kHz when driven by pressurized air. The supply air pressure (p_t) varies between $0.5 - 2.0$ psig. Far-field acoustic measurements in an anechoic chamber show that the peak frequency increases slightly with p_t. Two-dimensional CFD simulations of the baseline deterrent reveal that, in the p_t range explored here, the two resonating chambers of the whistle operate out-of-phase, and the peak frequency of pressure fluctuations in each resonator is about 12 kHz, which is half that of the far-field radiating ultrasound. This flow pattern, as well as the peak frequency, are found to be insensitive to variations in p_t. These findings suggest that the mechanism of ultrasound generation in the baseline deterrent is Helmholtz resonance.

The numerical prediction approach is validated with far-field acoustic measurements in an anechoic chamber. Three-dimensional CFD simulation results are used with the Ffowcs Williams-Hawkings acoustic analogy to predict far-field ultrasound radiation. Pressure power spectral density spectra, tonal sound pressure level (SPL) spectra, and polar directivity are compared. The tonal SPL levels agree well, although there are some discrepancies in directivity.

A six-whistle ultrasound deterrent is designed by geometrically scaling the baseline whistle. The whistles are 100%, 85%, 70%, 60%, 55%, and 50% of the size of the baseline whistle. The deterrent is fabricated, and the model is tested in the anechoic chamber over the supply air pressure range $2.0 \le p_t \le 10.0$ psig. As p_t increases above 5.0 psig, six dominant peaks are observed in the far-field ultrasound in the $20 - 50$ kHz range. The SPL values of the peaks reach 90 dB with a reference pressure of 20μpa at a distance 1.651 m away from the whistle when $p_t = 10$ psig.

The present work analyzes the flow/acoustics phenomena associated with the proposed deterrent. It is however limited in following aspects: (1) the transients effects of variations in supply pressure have not been considered, (2) the atmospheric attenuation effects are modeled empirically, and (3) the flow/acoustic interaction effects between multiple whistles in close proximity in a deterrent are not evaluated. In addition to removing the above limitations, future research directions include: (1) ability to modulate the intensity and frequency of the ultrasound from the deterrent, (2) couple near-field predictions with long-range acoustic propagation methods to estimate the SPL of the deterrent ultrasound on the ground, and (3) study the response of bats to the deterrent in a flight cage and in the field.

ACKNOWLEDGMENTS

DATA AVAILABILITY STATEMENT

The data that support the findings of this study are available from the corresponding author upon reasonable request.

Appendix A: Mesh refinement study

A mesh refinement study is carried out using the aerodynamic performance (total pressure loss) and radiated ultrasound (peak PSD) as metrics. The computational domain is divided into multiple regions for meshing. Region 1 includes the resonating chambers and the exit pipe. The areas around the sharp edges of the chamber openings are denoted Region 0. The channel (upstream of Region 1) is divided into regions 2, 3, and 4, with the cell size gradually increasing towards the inlet. Figure 21 shows the computational domain and identifies the different regions in which the cell sizes are varied for the mesh refinement study.
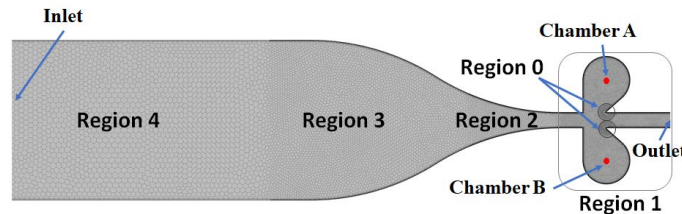

FIG. 21: The computational domain identifying the different mesh regions (0-4).

Four mesh sizes are considered – *Coarsest, Coarse, Baseline,* and *Fine* – with the names reflecting the mesh density variation. The average cell sizes in the different regions for the different meshes are listed in Table IV. Stagnation pressure $p_t = 2.0$ psig is prescribed at the inlet and the outlet is set to atmospheric pressure. Data probes in the center of the resonating chambers are used to record the unsteady pressure signal. Peak PSD of pressure is evaluated to assess the acoustic performance and the aerodynamic performance is measured via the loss of stagnation pressure (p_t) in the whistle. The results in Table IV suggest that the acoustic and aerodynamic performance are nearly insensitive if the mesh density is increased beyond the Baseline grid. The Baseline mesh is used for the numerical results in this paper.

TABLE IV: Settings for the mesh refinement study and results. Percent difference from the Baseline mesh results are shown in brackets.

Mesh	Region# & corresponding cell size (m)					Results	
	0	1	2	3	4	Peak PSD, dB/Hz	p_t loss, Pa
Coarsest	1.5E-4	3.0E-4	6.0E-4	9.0E-4	1.2E-3	154 (-0.6%)	10568 (+5.7%)
Coarse	1.0E-4	2.0E-4	4.0E-4	6.0E-4	1.0E-3	154 (-0.6%)	10638 (+6.4%)
Baseline	*0.5E-4*	*1.0E-4*	*2.0E-4*	*3.0E-4*	*5.0E-4*	*155*	*10000*
Fine	0.3E-4	0.5E-4	1.0E-4	1.5E-4	2.5E-4	155 (+0.0%)	10257 (+2.6%)

Appendix B: Theoretical estimates of frequencies in classical resonators

We provide theoretical estimates of frequencies corresponding to Helmholtz resonance, standing-wave cavity resonance, Rossiter modes[25] and pipe resonance mechanisms. A typical Helmholtz resonator[28] consists of a rigid-walled cavity of volume V neck area S and neck length L (Fig. 22). A Helmholtz resonator can be treated as a spring-mass dynamical system where the air in the neck serves as the system "mass" and the compressibility of the fluid (air) in the cavity plays the role of the "spring". The natural frequency of this
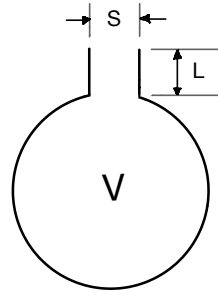
FIG. 22: A schematic of a Helmholtz resonator

system, f_{HR} can be expressed as

$$f_{HR} = \frac{c}{2\pi}\sqrt{\frac{S}{VL_s}}, \tag{B1}$$

where c is the speed of sound, L_s is the effective neck length. In the typical model, $L_s = L$, but in practical situations, L_s is obtained using L and a linear scale of the neck area[28,29]. For resonators in which the neck is formed of a thin wall i.e.,L is very small, Ma et al.[35] suggests using an "effective" neck length equal to the opening length of the neck to calculate f_{HR}. Taking $L_s = O$ for the resonators in the baseline whistle (see Fig. 2b), the f_{HR} is estimated to be 11.7 kHz.

The cavity closed by the shear layer can respond according to its box/cavity modes: standing waves in the longitudinal, crossflow (along the depth), and spanwise directions[24]. In our case, the depth-mode standing wave frequency, f_{SW}, is estimated using

$$f_{SW} = \frac{c}{2}\frac{n_{depth}}{2(L_{chamber} - t/2)}, \tag{B2}$$

where n_{depth} is an integer. When $n_{depth} = 1$, the estimated f_{SW} for the resonators of the baseline whistle is 15.3 kHz. Note that this equation assumes a rectangular cavity.

The frequencies of the Rossiter modes, f_{RM} are estimated using

$$f_{RM} = \frac{U}{O}\frac{n - \alpha}{(M + 1/\kappa)}, \tag{B3}$$

where α describes the phase delay between the hydrodynamic forcing and the acoustic feedback and κ is the convection velocity of the shear layer normalized by the free stream velocity, and n is an integer[26]. Since the flow Mach number (M) is small in our application, $\alpha = 0$. An empirical value of $\kappa = 0.5$ is used, and the flow speed (U) and M are obtained from CFD data acquired at the center of the whistle throat.

Appendix C: Rossiter modes

For the baseline design evaluated in this paper, the predicted first Rossiter's mode frequency coincides with the Helmholtz resonance frequency of the chamber in the range of supply pressure (p_t) tested. To separate these two frequencies, a whistle with a modified geometry (Fig. 23a) is simulated for $p_t = 0.5, 1.0, 1.5$ psig. The modified whistle chamber has a larger volume compared with the baseline design, reducing the

Helmholtz resonance frequency to 0.65 kHz; the length of the gap over the orifice (O) and the angle of the downstream edge (θ) edge are unchanged.

Figure 23b shows the variation with p_t of the predicted peak frequency at the center of the chamber. The expected frequencies corresponding to the first Rossiter mode and Helmholtz resonance are also plotted. The predicted chamber frequency closely follows the Helmholtz resonance frequency, indicating that Helmholtz resonance is the dominant mechanism here.
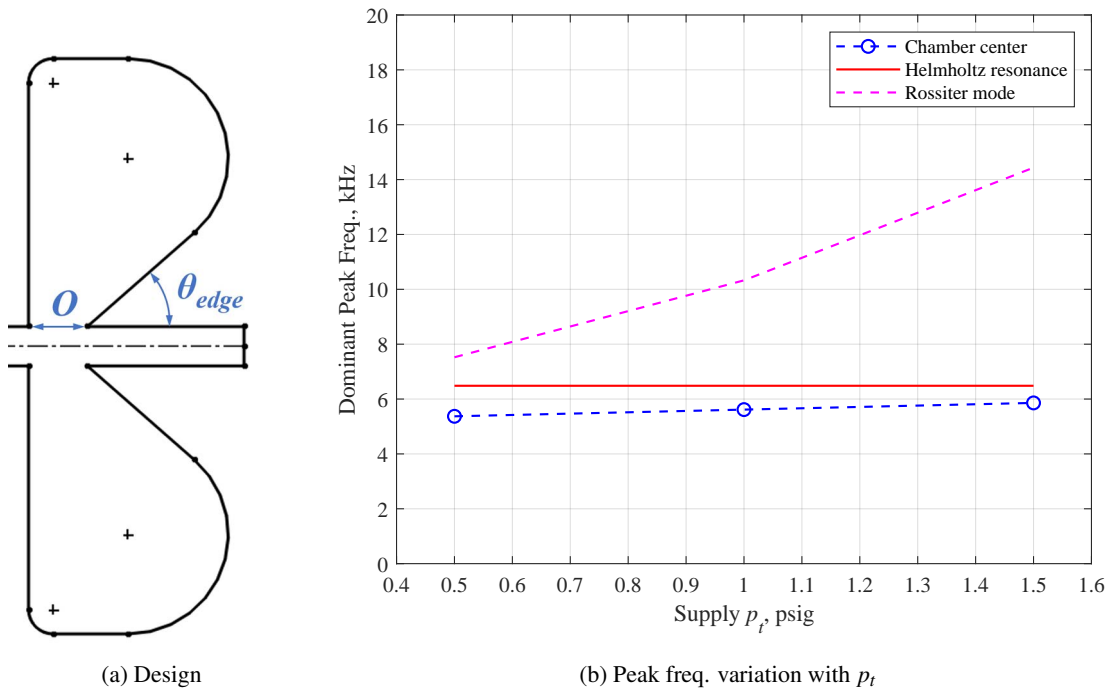

(a) Design

(b) Peak freq. variation with p_t

FIG. 23: Investigation of resonance mechanism – Helmholtz vs. Rossiter mode. Variation of peak chamber frequency with p_t shows the observed chamber frequency is closer to the theoretical Helmholtz resonance frequency.

REFERENCES

[1] B. B. Beeken, Fluid ultrasonic generator, 1969. US Patent 3,432,804.

[2] A. Rosenberg, S. Selvaraj, A. Sharma, A novel dual-rotor turbine for increased wind energy capture, Journal of Physics: Conference Series 524 (2014) 012078.

[3] B. Moghadassian, A. Rosenberg, A. Sharma, Numerical investigation of aerodynamic performance and loads of a novel dual rotor wind turbine, Energies 9 (2016) 571.

[4] H. Hu, Z. Wang, A. Ozbay, W. Tian, A. Sharma, An experimental investigation on the wake characteristics behind a novel twin-rotor wind turbine, in: 33rd Wind Energy Symposium, 2015, p. 1663.

[5] A. Rosenberg, A. Sharma, A prescribed-wake vortex lattice method for preliminary design of co-axial, dual-rotor wind turbines, Journal of Solar Energy Engineering 138 (2016).

[6] B. Moghadassian, A. Sharma, Inverse design of single-and multi-rotor horizontal axis wind turbine blades using computational fluid dynamics, Journal of Solar Energy Engineering 140 (2018).

[7] B. Moghadassian, A. Sharma, Designing wind turbine rotor blades to enhance energy capture in turbine arrays, Renewable Energy 148 (2020) 651–664.

[8] L. Chen, C. Harding, A. Sharma, E. MacDonald, Modeling noise and lease soft costs improves wind farm design and cost-of-energy predictions, Renewable Energy 97 (2016) 849–859.

[9] W. F. Frick, T. Kingston, J. Flanders, A review of the major threats and challenges to global bat conservation, Annals of the New York Academy of Sciences 1469 (2020) 5–25.

[10] N. A. Friedenberg, W. F. Frick, Assessing fatality minimization for hoary bats amid continued wind energy development, Biological Conservation 262 (2021) 109309.

[11] T. L. Cheng, J. D. Reichard, J. T. Coleman, T. J. Weller, W. E. Thogmartin, B. E. Reichert, A. B. Bennett, H. G. Broders, J. Campbell, K. Etchison, et al., The scope and severity of white-nose syndrome on hibernating bats in north america, Conservation Biology 35 (2021) 1586–1597.

[12] C. M. Martin, E. B. Arnett, R. D. Stevens, M. C. Wallace, Reducing bat fatalities at wind facilities while improving the economic efficiency of operational mitigation, Journal of Mammalogy 98 (2017) 378–385.

[13] E. B. Arnett, C. D. Hein, M. R. Schirmacher, M. M. Huso, J. M. Szewczak, Evaluating the effectiveness of an ultrasonic acoustic deterrent for reducing bat fatalities at wind turbines, PloS one 8 (2013).

[14] W. B. Romano, J. R. Skalski, R. L. Townsend, K. W. Kinzie, K. D. Coppinger, M. F. Miller, Evaluation of an acoustic deterrent to reduce bat mortalities at an illinois wind farm, Wildlife Society Bulletin 43 (2019) 608–618.

[15] S. P. Weaver, C. D. Hein, T. R. Simpson, J. W. Evans, I. Castro-Arellano, Ultrasonic acoustic deterrents significantly reduce bat fatalities at wind turbines, Global Ecology and Conservation 24 (2020) e01099.

[16] P. M. Gorresen, P. M. Cryan, D. C. Dalton, S. Wolf, J. A. Johnson, C. M. Todd, F. J. Bonaccorso, Dim ultraviolet light as a means of deterring activity by the hawaiian hoary bat lasiurus cinereus semotus, Endangered Species Research 28 (2015) 249–257.

[17] B. Huzzen, Does a Textured Coating Alter Bat Activity and Behavior in Proximity to Wind Turbine Towers?, Ph.D. thesis, Texas Christian University, 2019.

[18] R. E. Good, G. Iskali, J. Lombardi, T. McDonald, K. Dubridge, M. Azeka, A. Tredennick, Curtailment and acoustic deterrents reduce bat mortality at wind farms, The Journal of Wildlife Management (2022) e22244.

[19] M. R. Schirmacher, Evaluating the effectiveness of an ultrasonic acoustic deterrent in reducing bat fatalities at wind energy facilities, Technical Report, Bat Conservation International, Austin, TX (United States), 2020.

[20] J. W. Horn, E. B. Arnett, M. Jensen, T. H. Kunz, Testing the effectiveness of an experimental acoustic bat deterrent at the maple ridge wind farm, Report Prepared for: The Bats and Wind Energy Cooperative and Bat Conservation International, Austin, TX (2008).

[21] R. C. Chanaud, Aerodynamic whistles, Scientific American 222 (1970) 40–47.

[22] J. W. S. B. Rayleigh, The theory of sound, volume 2, Macmillan, 1896.

[23] T. Wilson, G. Beavers, M. DeCoster, D. Holger, M. Regenfuss, Experiments on the fluid mechanics of whistling, The Journal of the Acoustical Society of America 50 (1971) 366–372.

[24] X. Gloerfelt, Cavity noise, VKI lecture series 3 (2009).

[25] J. Rossiter, Wind-tunnel experiments on the flow over rectangular cavities at subsonic and transonic speeds, Technical Report R & M No. 3438, Aeronautical Research Council, Ministry of Aviation, 1966.

[26] G. J. Bennett, D. B. Stephens, F. Rodriguez Verdugo, Resonant mode characterisation of a cylindrical helmholtz cavity excited by a shear layer, The Journal of the Acoustical Society of America 141 (2017) 7–18.

[27] R. Henrywood, A. Agarwal, The aeroacoustics of a steam kettle, Physics of fluids 25 (2013) 107101.

[28] L. E. Kinsler, A. R. Frey, A. B. Coppens, J. V. Sanders, Fundamentals of acoustics, John wiley & sons, 1999.

[29] G. J. Ruijgrok, Elements of aviation acoustics, Delft University Press, 1993.

[30] J. E. Ffowcs Williams, D. L. Hawkings, Sound generation by turbulence and surfaces in arbitrary motion, Philosophical Transactions of the Royal Society of London. Series A, Mathematical and Physical Sciences 264 (1969) 321–342.

[31] F. R. Menter, Two-equation eddy-viscosity turbulence models for engineering applications, AIAA journal 32 (1994) 1598–1605.

[32] ISO 9613-1:1996, Calculation of the Absorption of Sound by the Atmosphere, Standard, International Organization for Standardization, 1995.

[33] H. E. Bass, L. C. Sutherland, A. J. Zuckerwar, D. T. Blackstock, D. Hester, Atmospheric absorption of sound: Further developments, The Journal of the Acoustical Society of America 97 (1995) 680–683.

[34] J. Szewczak, A. Corcoran, J. Kennedy, P. Ormsbee, T. Weller, Echolocation call characteristics of eastern us bats, Humboldt State University Bat Lab (2011).

[35] R. Ma, P. E. Slaboch, S. C. Morris, Fluid mechanics of the flow-excited helmholtz resonator, Journal of Fluid Mechanics 623 (2009) 1–26.